
2011-10

Raman and infrared phonon features in a designed cubic polymorph of CaTa2O6

Crystal Growth and Design,Washington, DC : American Chemical Society - ACS, v. 11, n. 12, p. 5567-5573, Oct. 2011
http://www.producao.usp.br/handle/BDPI/50063

CRYSTAL
GROWTH
& DESIGN

ARTICLE

pubs.acs.org/crystal

Raman and Infrared Phonon Features in a Designed Cubic Polymorph of $CaTa_2O_6$

N. G. Teixeira and R. L. Moreira*

Departamento de Física, ICEx, Universidade Federal de Minas Gerais, C.P. 702, 30123-970, Belo Horizonte, Minas Gerais, Brazil

R. P. S. M. Lobo

Laboratoire de Physique et d'Étude des Matériaux, ESPCI, CNRS, UPMC, 10 rue Vauquelin, F-75231 Paris Cedex 5, France

M. R. B. Andreeta and A. C. Hernandes

Instituto de Física de São Carlos, Universidade de São Paulo, C.P. 369, 13560-970, São Carlos, São Paulo, Brazil

A. Dias

Departamento de Química, ICEB, Universidade Federal de Ouro Preto, 35400-000, Ouro Preto, Minas Gerais, Brazil

Supporting Information

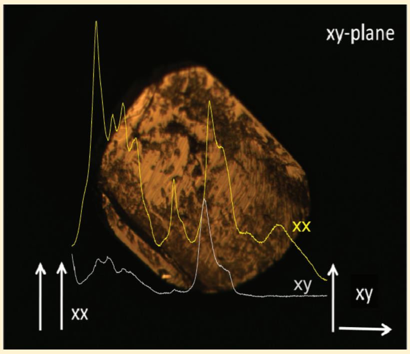

ABSTRACT: At room temperature, calcium tantalite ($CaTa_2O_6$) is known to exhibit three stable polymorphs, depending on the crystal growth conditions. In this work, the laser-heated pedestal growth method was used to obtain $CaTa_2O_6$ single crystal fibers in its quenched (ordered) cubic polymorph, attractive for optical applications. X-ray diffraction, Raman scattering and infrared spectroscopy showed that the fibers grew into the centrosymmetrical $Pm3$ space group. The growth axis was determined as [001]. The cylindrical fibers (20 mm long and 400 μm wide) showed good optical quality, without cracks or striations, but with small facets, parallel to crystal edges or to in-plane edge bicetrices. A comprehensive set of the optical phonons for this cubic structure was obtained, consisting of 13 (of 16 foreseen) triply degenerate polar phonons, and all the 21 predicted Raman modes. By using special scattering geometries, the Raman bands were attributed to their corresponding irreducible representations. In general, the phonons showed rather large damping constants, which do not compromise the designed optical applications in compact lasers but increase the losses in the microwave range, even though the dielectric response is quite adequate for microwave applications. Quenched defects and crystal polymorphism can be at the origin of the large phonon damping.

INTRODUCTION

Calcium tantalite ($CaTa_2O_6$) has been considered a good candidate for microwave and optical applications, owing to the adequate dielectric response shown at the microwave range,[1,2] and to the high optical transparency of single crystals along with the possibility to host rare-earth dopants which allow strong infrared optical emissions when pumped with visible light.[3−5] The underlying physical properties in each case are, nevertheless, dependent on the crystal structure adopted by the material, as usual. At room temperature, calcium tantalite can present three stable polymorphs, depending on the growth conditions: (i) a Ca-deficient simple cubic *perovskite* phase (half-occupied) with random occupation of vacancies on the A site, whose formula would be $Ca_{0.5}\square_{0.5}TaO_3$, obtained by low-temperature crystallization (below 650 °C); (ii) a quenched cubic phase with ordered Ca ions obtained from rapid crystallization from the melt; (iii) an orthorhombic *aeschynite* phase, obtained by slow crystallization or by annealing one of the cubic phases above 700 °C.[6−8] Two high temperature polymorphs were also reported (though the structures were not resolved yet) by Pivovarova et al.,[9] a tetragonal one between 1450 and 1650 °C, and a cubic phase from 1650 °C up to the melting point at about 1950 °C. All the mentioned phase transformations show kinetic behavior; that is, the phase transitions are not thermodynamically governed between the equilibrium states. They require annealing times as long as 50 h to be completed,[9] which indicates that large ionic movements are involved. Therefore, we can consider that all involved phases are indeed quite stable.

Received: August 28, 2011
Revised: September 30, 2011
Published: October 12, 2011

In view of the aforementioned microwave dielectric and optical applications, we shall concern the room temperature phases. Dielectric microwave ceramics are usually sintered at high temperatures for obtaining dense materials that optimize the dielectric response. In the case of $CaTa_2O_6$, ceramic materials prepared at about 1550−1600 °C and slowly cooled down to room temperature (cooling rates are typically 1−2 °C/min) yield the orthorhombic *aeschynite* structure (*Pnma* space group). The crystal structure,[7] microwave dielectric response,[1,2] and vibrational (through unpolarized Raman and infrared spectroscopies)[10] of the *aeschynite* $CaTa_2O_6$ polymorph have been previously reported. Although a complete determination of the phonon modes for this structure is still lacking, the published results are able to reasonably account for the main dielectric properties required for microwave applications of the material.

Concerning the room temperature cubic phases, very few works have been reported yet. Indeed, structural results on single crystals suggest that the disordered $Ca_{0.5}\square_{0.5}TaO_3$ phase (probably accompanied by CaO secondary phase) would belong to the ideal *perovskite* $Pm\bar{3}m$ group, with $a = 3.88$ Å and $Z = 1$ (one motif per unit cell).[6,7] To the best of our knowledge, there are no other reports on the physical properties of this phase, even though these references have been often cited by other authors.[8,9] On the other hand, the structure and the optical properties of the ordered (quenched) cubic phase of $CaTa_2O_6$ single crystals have been better explored. These materials were always obtained by laser-heated growth followed by fast cooling to room temperature. The crystal structure was determined as belonging to the $Pm3$ group, with $a = 7.78$ Å and $Z = 4$.[11] Concerning the optical and vibrational studies, it has been shown that the crystals are highly transparent in the visible range, but the reported Raman spectra showed very broad bands, suggesting possible cationic disorder, in contrast with structural results.[4] Moreover, Er^{3+}- and Nd^{3+}-doped single crystal fibers with the ordered cubic structure showed strong infrared emission, when pumped with visible light.[5,6]

In order to have a better understanding of the phonon behavior of the $CaTa_2O_6$ crystals, we have undertaken far-infrared and Raman scattering experiments on single crystal fibers obtained by the laser-heated pedestal growth (LHPG) method. In contrast to methods to grow bulk samples, this faster and less expensive technique is aimed at the growth of crystals of small diameters for optical applications, such as microlasers and other compact optical devices.[12−14] The purpose of the present work is to report a nearly complete phonon set of the $Pm3$ cubic polymorph of $CaTa_2O_6$, using single crystal fibers grown by the LHPG method. The results allow us to discuss the crystalline ordering of the material as well as the phonon contribution to the optical and dielectric responses of the system.

EXPERIMENTAL SECTION

$CaTa_2O_6$ single crystal fibers were obtained from pedestal rods (source and seed) using the LHPG setup described in detail in refs 15 and 16. In short, this system consists of a CO_2 heating laser of nominal power of 100 W, plane mirrors, a laser beam expander (Reflaxicon), a parabolic focusing mirror, and computer-controlled moving holders, for seed and source. Stoichiometric mixtures of the starting reagents, $CaCO_3$ (Riedel-de-Häen, 99%) and Ta_2O_5 (TEP, 99.99%), were ball milled for 24 h and used to prepare cylindrical pedestals (about 1.0 mm diameter and 50 mm long) by cold extrusion after adding a small amount of polyvinyl alcohol in aqueous solution (0.2 g/L). The green-rods were dried in air and used as seed and source in the growth process. The crystal growth occurred in air at 2040 ± 100 °C (the $CaTa_2O_6$ congruent melting point is ca. 1950 °C), using pulling rates of 1.6 mm/min (pedestal speed 0.44 mm/min), in the upward direction, without seed or pedestal rotation. The growth conditions were always very stable. Optically transparent single crystal fibers of $CaTa_2O_6$ were successfully obtained with average diameters of 400 μm and 20 mm long. The fibers were free of cracks or striations but contained small facets parallel to the cylindrical axis that helped us to orient the samples for the optical measurements.

In order to check the structural quality of the fibers and to determine the crystallographic orientations for the spectroscopic measurements, X-ray diffraction analyzes were performed in small crystals (0.8 mm long and 0.40 mm diameter) cut from the fibers, using a Gemini Oxford single crystal diffractometer equipped with a Mo−Kα source (45 kV, 40 mA). Data treatment was done with the CRYSALIS software. The X-ray results were compatible with an ordered $Pm3$ cubic phase, with a lattice parameter $a = 7.745$ Å. No secondary phase was detected. The growth direction was identified as nearly parallel to the [001] direction (= c), with an angular deviation smaller than 5°. The small facets have been shown to be normal to the [110] (main facets, henceforth diagonal d and d' directions) or to [100] (a or b) directions (minor facets). A view of the oriented crystal is shown in Figure S1 (Supporting Information). For the spectroscopic measurements, the samples had one longitudinal dz plane and the transversal xy surface polished to an optical grade.

Polarized infrared measurements were performed in a Fourier transform spectrometer (Nicolet Nexus 470), equipped with a Centaurus microscope (10× magnification, incident lightbeam with 350 μm diameter at the focus), from 50 to 4000 cm^{-1}. In the mid-infrared region (550−4000 cm^{-1}), we used the commercial configuration of the spectrometer, consisting of a SiC source, a Ge coated KBr substrate, a liquid-N_2-cooled HgCdTe detector, and a grid polarizer onto a ZnSe substrate. The spectra were collected under nitrogen purge, by averaging 32 scans, in observation regions of 300 μm × 300 μm, and preselected spectral resolution of 2 cm^{-1}. A gold mirror was used for the reference spectra. The far-infrared region (50−700 cm^{-1}) was attained by adapting the Centaurus microscope to receive a far-infrared detector (liquid-He-cooled Si-bolometer) and using a solid substrate Si-beam-splitter and a wire grid polarizer onto polyethylene substrate.[17] The external rear entrance of the spectrometer was used to receive the output signal of the bolometer. The measurements were recorded by averaging 128 scans with optimized (low) scan rates. The other experimental conditions were the same as for mid-infrared measurements. The reflectivity spectra obtained in mid- and far-infrared regions matched well (within 2%) in the superposition region (550−700 cm^{-1}).

Polarized micro-Raman scattering spectra were recorded using a *Jobin-Yvon* LABRAM-HR spectrometer equipped with a Peltier-cooled CCD detector and a confocal Olympus microscope (50× objective). The spectral resolution was ca. 1 cm^{-1} and the lateral resolution of 2 μm. The measurements were carried out in backscattering geometry, using the 632.8 nm line of a helium−neon laser as excitation source. Appropriate interference filter for rejecting laser plasma lines, edge filter for stray light rejection, polarizer, and half-wave plate were used.

RESULTS AND DISCUSSION

Polarized and unpolarized infrared reflectivity spectra on the polished dz-plane of the $CaTa_2O_6$ fiber were obtained under microscope, in the spectral region 50−4000 cm^{-1}. Figure S2 (Supporting Information) gives a photograph of the measured area of the sample. The results shown in Figure 1 (top curves) confirm the cubic symmetry of the $CaTa_2O_6$ single crystal fiber: the z-polarized (red line) and unpolarized (black line) spectra are essentially the same, which rules out the possibility of a lower symmetric phase. Therefore, in the sequence, only the unpolarized spectrum will be considered, once it presents a higher signal-to-noise ratio.

Once the cubic phase has been confirmed, we consider now the two possible cubic room-temperature phases. The Ca-deficient phase would belong to the ideal *perovskite* structure, which has only three infrared-active modes (and no first-order Raman-active mode), like in classical $SrTiO_3$.[18,19] This structure is not compatible with the large number of phonons seen in the infrared spectra in Figure 1. Therefore, we shall take the ordered *Pm*3 structure. In this case, Tiedemann and Müller-Buschbaum[11] have determined the crystal structure, including the atomic site positions (Wyckoff sites). Then, we used the factor-group method of Rousseau et al.[20] for determining the number and symmetries of the optical phonon modes. The results are given in Table 1, which shows that there would be 16 F_u infrared-active modes for this structure.

The unpolarized infrared reflectivity spectrum of $CaTa_2O_6$ was fitted by a nonlinear program, within the four-parameter semiquantum model.[21] In this framework, at quasi-normal incidence, the reflectivity (*R*) follows the Fresnel law

$$R = \left| \frac{\sqrt{\varepsilon(\omega)} - 1}{\sqrt{\varepsilon(\omega)} + 1} \right|^2 \qquad (1)$$

where the dielectric function, described in terms of four parameters that give the positions (Ω) and damping (γ) of the transverse (TO) or longitudinal (LO) polar phonon branches, is given by

$$\varepsilon(\omega) = \varepsilon_\infty \prod_{j=1}^{N} \frac{\Omega_{j,\mathrm{LO}}^2 - \omega^2 + i\omega\gamma_{j,\mathrm{LO}}}{\Omega_{j,\mathrm{TO}}^2 - \omega^2 + i\omega\gamma_{j,\mathrm{TO}}} \qquad (2)$$

In the above expression, ε_∞ gives the core (electronic) contribution and the sum is done over all the *N* polar modes.

The bottom curves of Figure 1 show the best fitting (blue solid line) of the experimental (unpolarized) infrared reflectivity data (open circles) by using eqs 1 and 2. The fitting of the infrared reflectivity spectra by the four-parameter semiquantum model gives the complete characteristics of the polar phonon of the system, which allows one to obtain the relevant optical (or dielectric) functions over all the measured spectral range. In the case of our cubic $CaTa_2O_6$ single crystal, the obtained dielectric functions are presented in the panels of Figure 2. In this figure, the top and middle panels present the real and imaginary part of the dielectric function (ε), while the bottom panel presents the imaginary part of the reciprocal dielectric constant ($\eta = \varepsilon^{-1}$). The TO and LO branches of each polar mode are the poles and zeros of Re(ε). However, the phonon positions and widths are more accurately determined from the peaks in Im(ε) and Im(η),

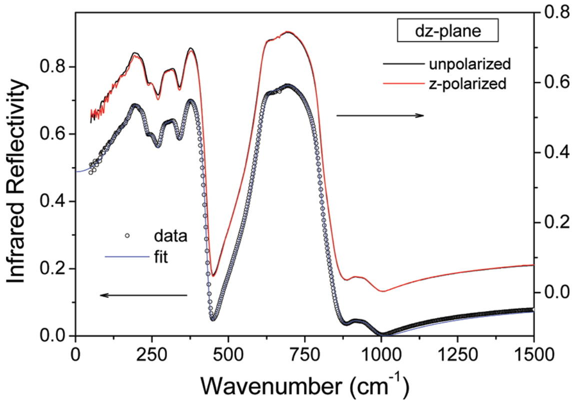

Figure 1. Infrared reflectivity spectra of the cubic $CaTa_2O_6$ single crystal fiber, recorded under a microscope, on the *dz* sample surface. The top curves show the *z*-polarized (red line) and unpolarized (black line) spectra. The bottom curves correspond to the unpolarized spectrum (black open circles) along with its fitting by the four-parameter semiquantum model (blue solid line).

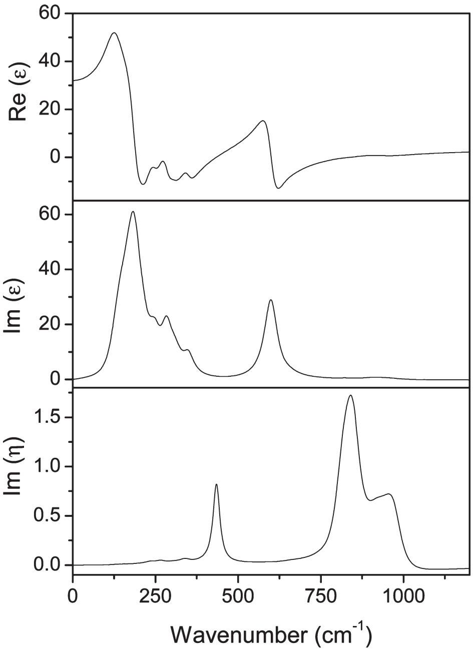

Figure 2. Real and imaginary part of dielectric constant (ε) and imaginary part of the reciprocal dielectric function (η), obtained through the fittings of the infrared reflectivity spectrum of the $CaTa_2O_6$ cubic sample by the four-parameter semiquantum model.

Table 1. Factor-Group Analysis for the $CaTa_2O_6$ *Pm*3 Cubic Symmetry (#200, or T_h^1)[a]

	ionic position[11]					
ion	X	Y	z	Wyckoff Site	site symmetry	site contribution
Ca_I	0.5	0.5	0.5	1b	T_h	F_u
Ca_{II}	0.5	0	0	3d	D_{2h}	$3F_u$
Ta	0.2475(2)	0.2475(2)	0.2475(2)	8i	C_3	$A_g \oplus A_u \oplus E_g \oplus E_u \oplus 3F_g \oplus 3F_u$
O_I	0.5	0.227(7)	0.284(8)	12k	C_s	$2A_g \oplus A_u \oplus 2E_g \oplus E_u \oplus 4F_g \oplus 5F_u$
O_{II}	0	0.273(7)	0.220(8)	12j	C_s	$2A_g \oplus A_u \oplus 2E_g \oplus E_u \oplus 4F_g \oplus 5F_u$

[a] $\Gamma = 5A_g\ (R) \oplus 5E_g\ (R) \oplus 11F_g\ (R) \oplus 16F_u\ (IR) \oplus 1F_u\ (acoust.) \oplus 3A_u\ (sil.) \oplus 3E_u\ (sil.)$.

Table 2. Infrared Dispersion Parameters, Dielectric Strengths ($\Delta\varepsilon_j$) and Loss Tangent Obtained from the Fitting of the Infrared Spectrum of the $CaTa_2O_6$ Ordered Cubic Crystal by the Four-Parameter Semiquantum Model[a]

mode	$\Omega_{j,\mathrm{TO}}$	$\gamma_{j,\mathrm{TO}}$	$\Omega_{j,\mathrm{LO}}$	$\gamma_{j,\mathrm{LO}}$	$\Delta\varepsilon_j$	$10^6 \tan\delta_j/\omega$
1	135.0	67.0	145.0	93.5	6.70481	776.80
2	190.0	55.9	215.5	39.5	11.35830	554.29
3	217.2	32.5	231.0	48.0	0.31791	6.90
4	252.8	41.0	264.0	35.0	1.59107	32.17
5	288.5	38.0	296.0	35.5	2.62522	37.77
6	301.0	62.0	339.8	36.0	1.78534	38.50
7	349.0	37.5	434.7	25.0	0.73388	7.12
8	600.0	49.0	646.0	59.0	2.41680	10.37
9	647.0	65.0	753.8	69.5	0.04340	0.21
10	755.0	67.5	811.0	67.0	0.00662	0.02
11	831.0	105.0	852.0	58.0	0.02446	0.12
12	902.0	73.5	917.0	80.0	0.03975	0.11
13	955.0	100.0	976.0	70.0	0.04346	0.15
	$16\ F_{1u}$: $\varepsilon_\infty = 4.04$; $\varepsilon_r = 31.7$; $Q_u \times f = 20.5$ THz					$\Sigma \tan\delta_j/\omega = 1466 \times 10^{-6}$

[a] The phonon positions and damping constants are given in cm^{-1}.

for the TO and LO branches, respectively. A very good description of the experimental data was obtained with 13 polar modes, whose characteristics are summarized in Table 2, besides the core contribution (ε_∞), dielectric strengths ($\Delta\varepsilon_j$), and losses ($\tan\delta_j$). We note first a reasonable agreement with group-theory predictions for the number of infrared modes of the *Pm*3 phase. The three missing modes are likely hidden by the observed rather broad modes. Indeed, as shown in Table 2, all depicted modes present large damping constants. Most important, the 13 observed modes contain the relevant information for describing the dielectric response of the system at the infrared region.

In addition, the phonon characteristics also allow estimating the dielectric behavior in the neighboring regions. First, we note that the ε_∞ value gives us a measurement of the refractive index of the crystal ($\varepsilon_\infty = n^2$), as 2.01, which is comparable to the values obtained for a $CaNb_2O_6$ orthorhombic *columbite* crystal (n between 1.97 and 2.22).[17] On the other hand, the intrinsic dielectric properties of an insulator centrosymmetrical material at microwave frequencies is entirely given by the phonon (and electronic) characteristics.[22] The static (microwave, $\Omega_{j,\mathrm{TO}} \gg \omega$) dielectric constant is given by the summing up the core contribution with the individual dielectric strengths ($\varepsilon_r = \varepsilon_\infty + \Sigma_j \Delta\varepsilon_j$) given by[21,22]

$$\Delta\varepsilon_j = \frac{\varepsilon_\infty}{\Omega^2_{j,\mathrm{TO}}} \times \frac{\prod\limits_k (\Omega^2_{k,\mathrm{LO}} - \Omega^2_{j,\mathrm{TO}})}{\prod\limits_{k\neq j} (\Omega^2_{k,\mathrm{TO}} - \Omega^2_{j,\mathrm{TO}})} \tag{3}$$

Besides, the dielectric loss tangent ($\tan\delta$) is given by adding the individual losses, that is,

$$\tan\delta = \sum_j \tan\delta_j = \sum_j \omega \frac{\Delta\varepsilon_j \gamma_{j,TO}}{\varepsilon_r \Omega^2_{j,TO}} \tag{4}$$

As it can be seen in Table 2, the six strongest modes (#1, 2, 4, 5, 6, and 8) contribute with more than 95% of the measured ε_r, as well as $\tan\delta$. Therefore, the dielectric contribution of the missing modes, which are either weaker or masked by such strong modes, can be neglected in the calculations. The values of the estimated static dielectric constant and unloaded quality factor ($Q_u = \cot\delta$) are given in Table 2. The meaning of the obtained results from the fundamental and applications point of views will be discussed later, after the Raman results are presented.

Table 3. Intensity of the Raman-Active Modes in Different Backscattering Configurations for Cubic Structures[a]

	irreducible representations		
configuration	A_g	E_g	$F_{2\ g}$
$z(xx)\bar{z}$	a^2	$4b^2$	0
$z(xy)\bar{z}$	0	0	d^2
$z(dd)\bar{z}$	a^2	$3b^2$	d^2
$z(dd')\bar{z}$	0	b^2	0

[a] The indicated directions are z // [001]; x // [100]; y // [010]; d // [110] and d' // [$1\bar{1}0$]. a, b, and d are elements of the Raman polarizability tensors.

According to the character table of the T_h point group, the *gerade* irreducible representations have the following quadratic base functions: $x^2 + y^2 + z^2$ (A_g), $x^2 + y^2 - 2z^2$ and $x^2 - y^2$ (E_g), xy, xz, and yz (F_g).[20] In order to attribute these modes to their respective irreducible representations, particularly to discriminate between modes of A_g and E_g symmetry, special scattering configurations should be used. In our polarized Raman experiments, we used four different backscattering geometries, namely, $z(xx)\bar{z}$, $z(xy)\bar{z}$, $z(dd)\bar{z}$, and $z(dd')\bar{z}$, which allowed us to completely discriminate the *gerade* modes of the $CaTa_2O_6$ cubic structure,[23] as it is indicated in Table 3. Here we use the classical Porto's notation for the scattering geometries;[24] for example, $z(xy)\bar{z}$ means that an incoming lightbeam propagating along the z direction and polarized along x excited the crystal, while the collected light along $-z$ was analyzed for y polarization.

Figure S3 (Supporting Information) shows in situ micrographs of the sample cross-section indicating the scattering geometries used. Table 3 presents the intensity elements linked to the different irreducible representations, for the chosen scattering geometries, which were obtained from the Raman polarizability tensor of cubic point-groups.[23] These intensities, besides the selection rules, are important to determine which modes are enhanced or weakened into the different scattering configurations.

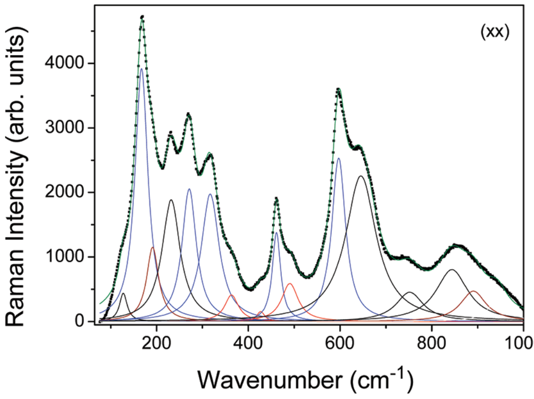

Figure 3. Raman spectrum of the $CaTa_2O_6$ ordered cubic crystal in the *xx* configuration (dots) and its adjustment with Lorentz lines (solid olive curve). For this configuration, we would expect $A_g \oplus E_g$ modes. The fitting Lorentz-type curves are in black (A_g), blue (E_g), and red (F_{2g} modes). Three additional modes, likely defect-activated infrared modes, are in wine.

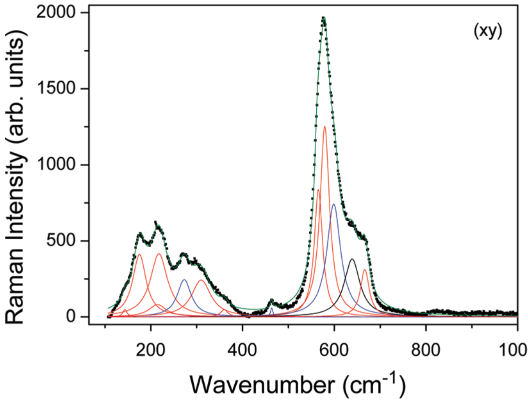

Figure 4. Raman spectrum of the $CaTa_2O_6$ ordered cubic crystal in the *xy* configuration (dots) and its adjustment with Lorentz lines (solid olive curve). For this configuration, only F_{2g} modes are predicted to appear. As before, the individual Lorentz-type curves are in black (A_g), blue (E_g), and red (F_{2g} modes). Note the enhancement of the F_{2g} modes.

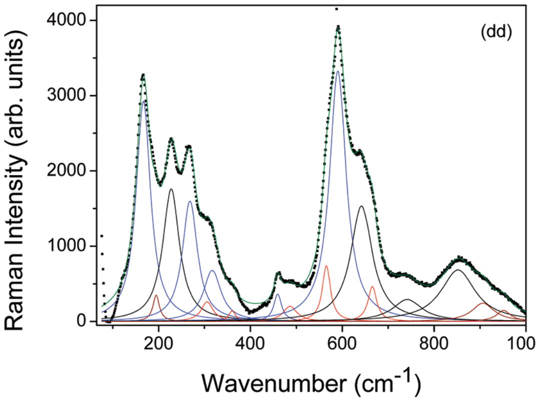

Figure 5. Raman spectrum of the $CaTa_2O_6$ ordered cubic crystal in the *dd* configuration (dots) and its adjustment with Lorentz lines (solid olive curve). For this configuration all *gerade* modes are predicted to appear. The individual Lorentz-type curves are in black (A_g), blue (E_g), red (F_{2g}), and wine (three defect modes also seen in Figure 3).

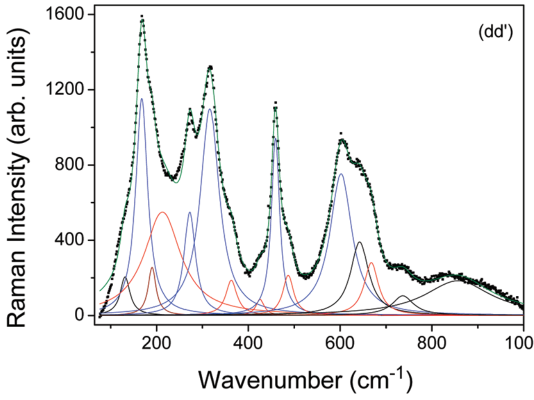

Figure 6. Raman spectrum of the $CaTa_2O_6$ ordered cubic crystal in the *dd′* configuration (dots) and its adjustment with Lorentz lines (solid olive curve). For this configuration, only E_g modes are predicted to appear. As before, the individual Lorentz-type curves are in black (A_g), blue (E_g), red (F_{2g}), and wine (one of the three precedent additional modes). Here, note the enhancement of the E_g modes.

The E_g and $F_{2\ g}$ modes are respectively the sole allowed modes for the $z(dd')\bar{z}$ and $z(xy)\bar{z}$ cross-configurations, respectively. The A_g modes are seen in both parallel configurations used; however, they are mixed with other modes. In the $z(dd)\bar{z}$ configuration, all modes are allowed, while for $z(xx)\bar{z}$, A_g modes are mixed only with E_g. In the first case, the E_g modes are slightly weaker than in the second one ($3b^2$ against $4b^2$).

The polarized Raman spectra, corrected by the Bose-Einstein thermal factor,[25] of the cubic $CaTa_2O_6$ crystal in the four chosen scattering configurations are presented in Figure 3 [$z(xx)\bar{z}$], Figure 4 [$z(xy)\bar{z}$], Figure 5 [$z(dd)\bar{z}$], and Figure 6 [$z(dd')\bar{z}$]. The spectra show a large number of first-order modes, ruling out any possibility for the ideal Ca-deficient *perovskite* structure. The polarization effects on these spectra are quite clear. We take benefit of the selection rules and intensity variations discussed above to discriminate between the symmetry of the modes. The spectra were fitted by Lorentz-type lines, shown in the figures, with colors corresponding to the attributed irreducible representation: black for A_g, blue for E_g, and red for F_{2g} modes. Three extra modes (wine) were seen in the $z(xx)\bar{z}$ and $z(dd)\bar{z}$ configurations, at about 190 cm^{-1}, 900 cm^{-1}, and 945 cm^{-1} (the first one of these modes was also seen in $z(dd')\bar{z}$). These are likely infrared modes that have been activated by defects.

The individual modes depicted by the Lorentz fittings for all scattering configurations are shown in Table S1 (Supporting Information). Now, by using the rules mentioned in Table 3, we present in Table 4 a summary of the attributed Raman modes for the cubic $CaTa_2O_6$ crystal. We note first that, despite the many leaks, all the 21 predicted *gerade* modes of this structure were observed and their corresponding symmetry was determined. The Raman modes are relatively broad, which could be due to remaining stresses in the sample because of the fast crystallization process used for producing the crystal fiber or to other quenched defects, such as cationic disorder. Finally, the present results show that the 10 *gerade* modes observed in the unpolarized Raman spectra of a $CaTa_2O_6$ fiber reported in ref 3 (not resolved by polarization) are indeed the five E_g, four A_g (they missed the 741 cm^{-1} mode), and one F_{2g} (360 cm^{-1}) modes, as seen here. The fact that those authors practically did not see the F_{2g} mode is linked to the arbitrary geometry used in their work.

Table 4. **Summary of the Depicted Raman Modes of the Cubic $CaTa_2O_6$ Crystal, with the Symmetry Attributions (Phonon Wavenumbers and Half Widths at Half-Maxima Are Given in cm^{-1})**

A_g	E_g	F_{2g}
126.8 (9.0)	167.8 (16.5)	146.7 (5.5)
227.2 (19.0)	272.3 (19.7)	175.1 (17.7)
641.8 (28.7)	316.8 (22.9)	214.6 (23.0)
741.6 (29.9)	459.3 (10.4)	217.8 (22.8)
850.2 (43.5)	601.8 (29.1)	309.9 (25.2)
		360.0 (9.4)
		425.5 (10.7)
		485.9 (17.2)
		565.2 (10.9)
		579.1 (12.7)
		667.3 (11.5)

As a whole, we have observed a quite complete set for the Raman and infrared spectra of an ordered cubic $CaTa_2O_6$ crystal. The infrared missing modes, 3 from 16, must have negligible contribution for the dielectric response of the system at the infrared and neighboring regions. All the 21 Raman modes were observed in polarized resolved spectroscopic analyses and their symmetries were determined. Raman and infrared modes are quite broad. This has been attributed to quenched stresses or defects because of the fast cooling process. In view of potential optical applications of this material as near-infrared or up-conversion lasers, such structural disorder does not constitute a problem, once it favors the tuning conditions (by broadening the infrared and visible absorption spectra), as indeed observed in ref 5.

Concerning the infrared modes, line broadening is responsible for decreasing the dielectric quality factor. $CaTa_2O_6$ ceramics are being considered for microwave applications. Owing to the preparation conditions, these materials belong to the orthorhombic *aeschynite* structure. Although the results presented here are for the ordered cubic phases of $CaTa_2O_6$, let us compare our intrinsic dielectric data extrapolated to the microwave region ($\varepsilon_r = 31.7$ and $Q_u \times f = 20.5$ THz) with direct microwave data obtained in the orthorhombic ceramics ($\varepsilon_r = 28.3$ and $Q_u \times f = 30.8$ THz, ref 2). The obtained (high) dielectric constant and quality factors are adequate for microwave applications, but the quality factors are relatively low compared with values shown by orthorhombic $CaNb_2O_6$ with *columbite* structure.[1,2,17,26] Conversely to tantalite *perovskites*, which have higher Q_u than niobate ones, the AB_2O_6 tantalites (B = Ta, A = divalent cation) have lower Q_u than corresponding niobates (B = Nb).[1,27] The polymorphism presented by members the tantalite family[1] could be at the origin of such behavior, since the ANb_2O_6 compounds with different A^{2+} cations have usually the *columbite* structure.

CONCLUSIONS

Optically transparent single crystal fibers of calcium tantalite have been obtained by the LHPG method. X-ray diffraction, Raman scattering, and infrared spectroscopy confirmed that the fibers grew into the *Pm*3 ordered cubic polymorph. Owing to the small sample dimensions (400 μm diameter), infrared and Raman spectroscopy were done under a microscope. The selection rules for Raman and infrared modes were well respected, confirming the good quality of the samples. We were able to determine a quite complete set of the optical phonon modes of the material in the structure: the 13 (of the predicted 16) most relevant (infrared) polar phonons and all the 21 predicted Raman modes. Special scattering geometries allowed attributing the Raman modes to their corresponding irreducible representations. In general, the phonons showed large damping constants, which do not compromise optical applications in designed compact lasers, but increase the losses in the microwave range, even though the dielectric response is quite adequate for microwave applications. Quenched defects and crystal polymorphism can be at the origin of this phonon behavior.

ASSOCIATED CONTENT

Ⓢ Supporting Information. Micrographs of the crystal fiber oriented for X-ray diffraction, infrared and Raman measurements are presented along with Raman fitting data for all configurations shown in the text. This material is available free of charge via the Internet at http://pubs.acs.org.

AUTHOR INFORMATION

Corresponding Author

*Telephone: +55.31.34095624; fax: +55.31.34095600; e-mail: bmoreira@fisica.ufmg.br.

ACKNOWLEDGMENT

The authors are grateful to Dr. Carlos Basílio Pinheiro for his help in the X-ray measurements and to the Brazilian agencies CNPq, FINEP, FAPEMIG, and FAPESP, for partially funding this work.

REFERENCES

(1) Lee, H. J.; Kim, I. T.; Hong, K. S. *Jpn. J. Appl. Phys. Part 2* **1997**, *36*, L1318.

(2) Kan, A.; Ogawa, H. *Jpn. J. Appl. Phys.* **2008**, *47*, 7716.

(3) Ferrari, C. R.; de Camargo, A. S. S.; Nunes, L. A. O.; Hernandes, A. C. *J. Cryst. Growth* **2004**, *266*, 475.

(4) De Camargo, A. S. S.; Ferrari, C. R.; Hernandes, A. C.; Nunes, L. A. O. *J. Phys.: Condens. Matter* **2004**, *16*, 5915.

(5) De Camargo, A. S. S.; Ferrari, C. R.; Silva, R. A.; Nunes, L. A. O.; Hernandes, A. C.; Andreeta, J. P. *J. Lumin.* **2008**, *128*, 223.

(6) Janhberg, L. *Acta Chem. Scand.* **1959**, *13*, 1248.

(7) Janhberg, L. *Acta Chem. Scand.* **1963**, *17*, 2548.

(8) Pivovarova, A. P.; Strakhov, V. I.; Smirnov, Yu. N. *Russ. J. Appl. Chem.* **1998**, *71*, 1497.

(9) Pivovarova, A. P.; Strakhov, V. I.; Smirnov, Yu. N. *Inorg. Mater.* **1999**, *35*, 1291.

(10) Repelin, Y.; Husson, E.; Dao, N. Q.; Brusset, H. *Spectrochim. Acta* **1979**, *35A*, 1165.

(11) Tiedemann, P.; Müller-Buschbaum, Hk. *Z. Anorg. Allg. Chem.* **1984**, *516*, 201.

(12) Feigelson, R. S. *J. Cryst. Growth* **1986**, *79*, 669.

(13) Feigelson, R. S. *Mater. Sci. Eng., B* **1988**, *1*, 67.

(14) Rudolph, P.; Fukuda, T. *Cryst. Res. Technol.* **1999**, *34*, 3.

(15) Hernandes, A. C. In *Recent Research Developments in Crystal Growth Research*; Trivandrum: Transworld Research Network, 1999; p 123.

(16) Andreeta, M. R. B.; Hernandes, A. C. In *Springer Handbook of Crystal Growth*; Dhanaraj, G., Byrappa, K., Prasad, V., Dudley, M., Eds.; Springer Berlin: Heidelberg, 2010; p 393.

(17) Teixeira, N. G.; Moreira, R. L.; Andreeta, M. R. B.; Hernandes, A. C.; Dias, A. *Cryst. Growth Des.* **2011**, *11*, 3472.

(18) Spitzer, W. G.; Miller, R. C.; Kleinman, D. A.; Howarth, L. E. *Phys. Rev.* **1962**, *126*, 1701.

(19) Nilsen, W. G.; Skinner, J. G. *J. Chem. Phys.* **1968**, *48*, 2240.

(20) Rousseau, D. L.; Bauman, R. P.; Porto, S. P. S. *J. Raman Spectrosc.* **1981**, *10*, 253.

(21) Gervais, F.; Echegut, P. In *Incommensurate Phases in Dielectrics*; Blinc, R., Levanyuk, A. P., Eds.; North Holland: Amsterdam, 1986; p 337.

(22) Petzelt, J.; Kamba, S. *Mater. Chem. Phys.* **2003**, *79*, 175.

(23) Ayala, A. P.; Paschoal, C. W. A.; Guedes, I.; Paraguassu, W.; Freire, P. T. C.; Mendes Filho, J.; Moreira, R. L.; Gesland, J.-Y. *Phys. Rev. B* **2002**, *66*, 214105.

(24) Otaguro, W. S.; Wiener-Avnear, E.; Arguello, C. A.; Porto, S. P. S. *Phys. Rev. B* **1971**, *4*, 4542.W.

(25) Hayes, W. Loudon, R. *Scattering of Light by Crystals*; Wiley-Interscience: New York, 1978.

(26) Pullar, R. C.; Vaughan, C.; Alford, N. M. *J. Phys. D: Appl. Phys.* **2004**, *37*, 348.

(27) Pullar, R. C. *J. Am. Ceram. Soc.* **2009**, *92*, 563.